Research Article

Anomalies in the short-range local environment and atomic diffusion in single crystalline equiatomic CrMnFeCoNi high-entropy alloy

Alevtina Smekhova[1] (✉), Daniel Gaertner[2], Alexei Kuzmin[3], Ana Guilherme Buzanich[4], Goetz Schuck[1], Ivo Zizak[1], Gerhard Wilde[2], Kirill V. Yusenko[4], and Sergiy Divinski[2] (✉)

[1] *Helmholtz-Zentrum Berlin für Materialien und Energie (HZB), D-12489 Berlin, Germany*
[2] *Institute of Materials Physics, University of Münster, D-48149 Münster, Germany*
[3] *Institute of Solid State Physics, University of Latvia, LV-1063 Riga, Latvia*
[4] *Bundesanstalt für Materialforschung und – prüfung (BAM), D-12489 Berlin, Germany*

© The Author(s) 2024

ABSTRACT

Multi-edge extended X-ray absorption fine structure (EXAFS) spectroscopy combined with reverse Monte Carlo (RMC) simulations was used to probe the details of element-specific local coordinations and component-dependent structure relaxations in single crystalline equiatomic CrMnFeCoNi high-entropy alloy as a function of the annealing temperature. Two representative states, namely a high-temperature state, created by annealing at 1373 K, and a low-temperature state, produced by long-term annealing at 993 K, were compared in detail. Specific features identified in atomic configurations of particular principal components indicate variations in the local environment distortions connected to different degrees of compositional disorder at the chosen representative temperatures. The detected changes provide new atomistic insights and correlate with the existence of kinks previously observed in the Arrhenius dependencies of component diffusion rates in the CrMnFeCoNi high-entropy alloy.

KEYWORDS

high-entropy alloys, diffusion, short-range order, extended X-ray absorption fine structure (EXAFS), reverse Monte Carlo

1   Introduction

Multi-component systems continuously attract the close attention of researchers from a wide range of disciplines due to a variety of phenomena observed through either non-ordinary macroscopic behaviour or exquisite local atomic interactions. High-entropy alloys (HEAs) composed of at least five principal components with nearly equiatomic concentrations [1, 2] represent a class of materials with unique macroscopic properties attractive for technological applications (e.g., Refs. [3–23]), and at the same time, they stimulate new approaches in disentangling their intricate local structure responsible for such behaviour.

The atomic heterogeneity of HEAs related to their chemical complexity at the atomic scale provokes strong variations in the local coordination of constituting elements, influencing valence electron concentration [24], lattice distortions [25–33], magnetic moments and relative magnetic couplings of components [27, 34–36], component-specific structural displacements [33, 35, 37, 38], activation energies and enthalpies of vacancy creation [39], a possibility to form locally ordered structures [40, 41], etc. These variations are already established to be a foundation for many diverse macroscopic properties of HEAs. It is widely accepted that at least at high temperatures the high-entropy alloys are considered to feature fully random solid solutions [1, 2], although they have to decompose in phase mixtures along with decreasing the temperature as thermodynamic calculations predict [42].

Nevertheless, such a decomposition is strongly slowed down by kinetic reasons and was observed after long annealing, e.g., for five hundred days at 773 K [43].

Slow diffusion mobility of principal components in HEAs as compared to pure metals, conventional alloys, and less compositionally complex counterparts was considered as one of HEAs "core effects" [1, 44]. It was hypothesised to be related to a strong heterogeneity of local environments formed by primary arrangements of atoms [44]. However, the sluggish diffusion concept as a "core effect" was recently demystified [45] accounting for the results of direct tracer measurements [46–51]. The radiotracer measurements provided direct evidence that atomic diffusion can be somewhat retarded in face-centered cubic (fcc) lattice [47, 49], slightly enhanced in body-centered cubic (bcc) ones [50], or even significantly, by orders of magnitude, enhanced in hexagonal close-packed (hcp) lattices [51] with respect to the diffusion rates in corresponding unaries.

In general, understanding the diffusion rates and diffusion mechanisms of individual components in HEAs is crucial due to the potential applications of HEAs as high-temperature materials and coatings. Up to now, the diffusion phenomena were mainly studied in the equiatomic CrMnFeCoNi alloy (commonly called "Cantor alloy") and its quaternary family both experimentally and theoretically [44, 46–48, 52–57] (see also the review article [58] and references therein), whereas experimental studies were done

---

by either inter- or tracer-diffusion techniques for polycrystalline and single-crystalline HEAs. Only limited data were published on non-fcc HEAs [50, 51].

The vast majority of the published diffusion data features the Arrhenius-type temperature dependence for the HEA-constituting elements [45], mainly because the measurements were typically performed in limited temperature intervals at high temperatures. Recently, radiotracer measurements of element diffusion in single crystalline CrMnFeCoNi alloy were performed over an extended temperature interval down to the temperatures below the predicted stability of the fcc solid solution [57]. For the first time, strong deviations from the Arrhenius-type temperature dependence of diffusion were observed, pointing towards the potential development of a short-range order with changing temperature [57]. These results have prompted the current study.

Preparation of HEA single crystals is a challenging task in materials science, and successful fabrication of single-crystalline HEAs together with peculiarities of the chosen preparation routes has already been reported, e.g., for the fcc $Al_{0.3}$CrFeCoNi [59, 60], fcc CrMnFeCoNi [56, 57, 61–63], bcc CrMnFeCoAl [64], fcc NiCoCrAlTiTaNbMoWC (with $L1_2$ ordered precipitates) [65], bcc HfNbTaTiZr (though, a polycrystal with mm-large grains) [66], and a novel Co-rich CoNiAlTaCrTi-type $L1_2$-strengthened single-crystal HEA [67]. Due to the elimination of the adverse effects of grain boundaries, single-crystalline HEAs are extremely attractive for finding the fundamental correlations between their functional properties and local atomic structures.

X-ray absorption spectroscopy combined with the reverse Monte Carlo (RMC) simulations enables an advanced and unbiased structural characterization of multi-component materials down to the atomic scale, being beneficial for unravelling the similarities and differences in the local environment of individual components. It can provide insights into the primary arrangements of atoms and trigger an understanding of their roles in certain macroscopic properties. Despite some natural limitations of the RMC approach to studies of 3d-elements-based HEAs, which do not allow the discussions of the atomic short-range ordering in the system, many other advantages of the RMC method were already testified. Examples of detailed element-specific studies of HEAs on the local scale with the use of the extended X-ray absorption fine structure (EXAFS) spectroscopy combined with RMC-based analysis can be found in our previous works [35, 36, 38].

Herein, we apply multi-edge EXAFS spectroscopy along with RMC simulations to explore element-specific local coordinations and component-dependent structure relaxations in single crystalline equiatomic face-centered cubic CrMnFeCoNi high-entropy alloy as a function of the annealing temperature. Specific features identified in atomic configurations of particular principal components for considered temperatures were correlated with previously observed [57] discontinuities in the Arrhenius dependencies of component diffusion rates. The present measurements are performed on the same samples (the same batch) used in the tracer diffusion studies [56, 57].

2 Experimental

2.1 Samples

The equiatomic CrMnFeCoNi single crystals were grown using the modified Bridgman technique under a purified Ar atmosphere with a slight surplus of Mn in the research group of Prof. Y. Chumlyakov (Tomsk State University, Russia).

The as-prepared single crystals were carefully etched to prevent undesirable contaminations and homogenized by annealing at

1473 K for 50 h. Subsequently, cylindrical samples of 8 mm in diameter were cut and sliced into 1.5 mm thick discs by spark erosion, and etched carefully again with aqua regia. One face of the specimen was polished by a standard metallographic procedure to a mirror-like quality. As a next step, the prepared samples were sealed in a silica glass tube under a purified Ar atmosphere (5 N), annealed at 1373 K for 3 days, and slowly cooled down to room temperature (RT) to remove the stresses induced by polishing. This procedure is identical to that used for the tracer diffusion studies before [56, 57], and guarantees compatibility of the results. The samples prepared in such a way reveal a homogeneous microstructure with a near-equilibrium concentration of point defects.

Since specific discontinuities (kinks) in the Arrhenius-type temperature dependencies of tracer diffusion for the constituent elements were observed at about 1000 to 1150 K [57] (see next section for more details), two characteristic states were intentionally prepared for the current EXAFS spectroscopy studies to represent the local environment above and below the revealed critical temperature interval. A low-temperature (LT) annealed state has been produced from the initially homogenized samples by long-term annealing at 993 K for 14 days. Afterwards, further annealing was performed at 1373 K to get a high-temperature (HT) state that represents the initial homogenized state described above. After annealing at temperatures related either to the LT or HT states the samples were cooled down to RT by quenching in cold water.

The chemical composition and the orientation of the prepared single crystals were checked by energy dispersive X-ray (EDX) spectroscopy and electron backscatter diffraction (EBSD), correspondingly. The growth direction of the particular batch corresponded to the [001] crystallographic direction with the sub-grain sizes above 500 μm and the misorientation spread of the mosaic structure within ±3°, see Fig. 1. Figure 1 confirms the chemical homogeneity and the single crystallinity of the samples, at least on the micrometer scale. This homogeneity was found to be not affected by annealing at 993 K corresponding to the LT state.
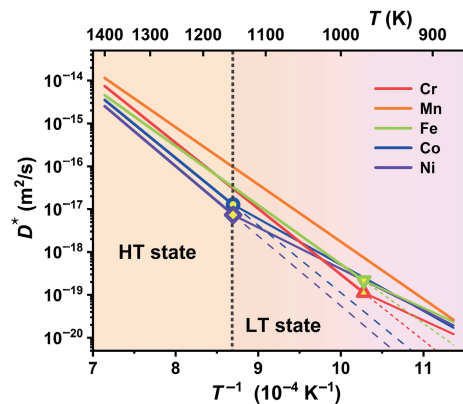
2.2 Diffusion of principal components

Self-diffusion of all constituting elements in single crystalline CrMnFeCoNi has been studied in detail in our previous works [56, 57] applying a radiotracer technique, which is considered the most direct and reliable technique for bulk diffusion measurements [68]. Exemplary, tracer self-diffusion has been measured along [001] and [111] crystallographic directions, and the absence of a diffusion anisotropy—as it is expected for the crystals with cubic symmetry and as it has to hold for true volume diffusion [69]—has been verified [56].

The subsequent measurements by Gaertner et al. [57] have been performed on the near [001] oriented single crystal (Fig. 1), applying the available ^{57}Co, ^{51}Cr, ^{59}Fe, ^{54}Mn, and ^{63}Ni radioisotopes. The diffusion rates, D^*, have been measured in a relatively extended temperature interval from $T = 1373$ K down to $T = 923$ K, and distinct deviations from the expected Arrhenius-type temperature dependencies, $\ln D^* \sim 1/T$, have been found, see Fig. 2. The characteristic kinks, i.e., the deviations from the otherwise linear Arrhenius-type temperature dependencies established for the high-temperature range, 1200–1373 K, appear for individual principal components at different critical temperatures. In fact, the relatively "slow" diffusing elements (Ni and Co), i.e., the elements with the smallest values of D^* at high temperatures, reveal the kinks at about 1150 K, whereas diffusion of moderately "fast" elements, i.e., of Cr and Fe, is characterized by the kinks at temperatures lower than 1000 K (Fig. 2). The "fastest" element,
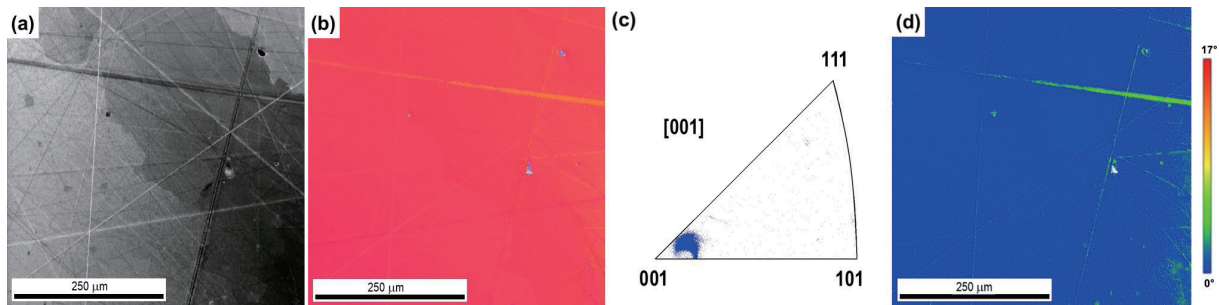
Figure 1 Microstructure of [001] CrMnFeCoNi single crystal after annealing at 1373 K for 3 days. From left to right: (a) original SEM image, (b) inverse pole figure (IPF) map, (c) IPF showing the orientation distribution of planes normal to the sample surface, and (d) the kernel average misorientation map.

Figure 2 Temperature dependencies of the tracer self-diffusion coefficients D^* for individual principal components in the CrMnFeCoNi single crystal with [001] growth direction [56, 57]. The dashed lines indicate the linear extrapolation of the high-temperature Arrhenius-type dependencies for each component; the vertical dotted line highlights the border between the HT and LT temperature regions mentioned in the present work. The critical temperatures found for Cr, Fe, Co, and Ni constituents are pointed out by open symbols. It should be noted, that the tracer diffusion technique involves measuring self-diffusion coefficients D^* at RT after annealing the species at a specified temperature followed by rapid quenching; the shown dependencies are based on the experimental temperature points taken at 1373, 1253, 1153, 1063, 993, and 923 K.

i.e., Mn, does not show any peculiarity in its Arrhenius-type temperature dependence in the whole temperature interval under investigation [57]. Note that the above classification of the elements in relatively "slow" and relatively "fast" is based on the diffusion behavior established at temperatures above 1200 K, and is conformed with the previous independent measurements of tracer self-diffusion in polycrystalline materials [46, 47]. The observed discontinuities in the tracer diffusion rates were qualitatively discussed in terms of contaminant changes of the short-range order (SRO) at lower temperatures due to known phase decomposition tendencies for the fcc solid solution phase [57].

2.3 X-ray absorption spectroscopy at the K absorption edges of 3d components

X-ray absorption spectra from both states of the single crystal were recorded at the K absorption edges of Cr (5.99 keV), Mn (6.54 keV), Fe (7.11 keV), Co (7.71 keV), and Ni (8.33 keV) by measuring fluorescent yield (FY) after the initial excitation by horizontally polarized X-ray photons.

The spectra from the crystal in the LT annealed state were recorded at 295 K in air at the BAMline [70, 71] of the BESSY II synchrotron radiation facility operated by Helmholtz–Zentrum Berlin (HZB), where hard X-rays from a 7 T wavelength shifter (WLS) were used. The sample was fixed in the X-ray beam between two 50-μm Kapton foils and the fluorescence signal was

detected in the backscattering geometry, using a custom-made four-element energy-dispersive Silicon drift detector [71, 72]. The X-ray flux on the sample was in the range of ~ 10^9 photons/s.

The spectra from the crystal in the HT annealed state were recorded at 295 K in the vacuum-pumped Cryo-EXAFS end-station [73] installed at the KMC-3 beamline [74] at HZB. X-ray fluorescence from the sample was recorded with a large-area energy-resolving 13-element Si-drift detector (Rayspec) equipped with the air/water-cooled Be-window. The X-ray flux from a bending magnet was ~ 10^{10} photons/s. The sample was fixed in the X-ray beam between two 50-μm thick Kapton foils in the 45° incident geometry. The collected fluorescence signal was normalized on the intensity of incoming X-ray photons, dead-time corrected, and integrated over the channels of the detector with the use of in-house software.

Before performing the qualitative frequency analysis by wavelet transforms (WTs) of the EXAFS spectra $\chi(k)k^2$ and much more precise RMC analysis, the raw data were pre-processed (in terms of necessary normalization, corrections, and integration) and averaged over the individual channels of the corresponding fluorescence detectors. No signatures of the radiation damage were observed in absorption spectra recorded at the K-edges of the constituents; the influence of different experimental geometries on the self-absorption effects was found to be negligible in the energy range important for the fitting procedure. For RMC analysis, EXAFS spectra $\chi(k)k^2$ at the K-edges of Cr, Mn, Fe, Co, and Ni were extracted from the averaged raw data using a conventional procedure [75] implemented in the XAESA code [76]. The EXAFS spectra of both—LT and HT annealed—HEA samples recorded at the K absorption edges of all five 3d elements (Cr, Mn, Fe, Co, and Ni) were used in the RMC simulations.

2.4 Wavelet transforms analysis

The qualitative analysis of EXAFS oscillations $\chi(k)k^2$ for each component was performed using the Morlet WTs [77]. The wavelet transformation allows one to visualize the behavior of the EXAFS spectra in both k and R spaces that can be employed to distinguish contributions from various atoms having different backscattering amplitudes [77]. Therefore, the WT provides more detailed information than the conventional Fourier transform (FT). Thus obtained WTs were used for the illustration of similarities and differences hidden in frequency patterns related to the local environment around each type of absorber and for highlighting existing peculiarities of the local structure around Ni and Mn absorbers in the LT and HT annealed states of the single crystalline HEA, correspondingly.

2.5 RMC simulations

An advantage of the RMC-based data analysis is the possibility to unbiasedly fit one and the same structural model simultaneously to several EXAFS spectra collected at the X-ray absorption edges of the main components present in a multi-component system

[35, 36, 38]. Here, we employed the RMC simulations as implemented in the EvAX code [78, 79]. The method uses the WTs for the comparison between the experimental and calculated EXAFS spectra simultaneously in *k* and *R* spaces [77] and the evolutionary algorithm (EA) for the acceleration of the optimization procedure [79].

The analysis requires generating the initial structural model of the material represented by a simulation box constructed as a supercell based on a repeating unit cell obtained from X-ray diffraction data with the imposed periodic boundary conditions (PBC) to avoid surface-related effects. The total number of atoms in the simulation box is given by the density of the material. During the RMC simulations, the volume and the shape of the simulation box remain fixed, while each atom is randomly displaced around its initial position in the ideal crystallographic lattice to account for the thermal and static disorders. The configuration-averaged (CA) EXAFS spectra are then calculated over all absorbing atoms of the same type located in the simulation box within the multiple-scattering (MS) formalism. At each iteration of the RMC simulations, the difference between WTs of the experimental and CA-EXAFS spectra for each X-ray absorption edge is evaluated and used as a criterion for the optimization of the structural model [78, 79].

The benefits of the RMC method as compared to conventional multi-shell EXAFS analysis become evident when the precise reconstruction of the local environment within the extended region beyond the first coordination shell around the absorbing atom is needed. The conventional approach requires the use of a huge number of model parameters to account for the contributions from atoms located in the distant coordination shells to the EXAFS spectrum due to the rapidly increasing number of scattering paths. To overcome this difficulty, additional assumptions and restrictions on the interdependences between the model parameters are usually introduced [75]. On the contrary, at each step of the RMC simulation, the CA-EXAFS spectrum is uniquely determined by the coordinates of atoms in the simulation box and can be accurately evaluated considering the MS effects. This makes it possible to account for the contributions from distant and overlapping coordination shells in the most unbiased manner. In this work, RMC simulations were applied to EXAFS spectra collected at the K absorption edges of all five constituents (Cr, Mn, Fe, Co, and Ni) of the single crystalline HEA.

The simulation box was built as a $4a \times 4a \times 4a$ supercell employing the PBC with the experimental value of the fcc lattice parameter $a = 3.61$ Å estimated by X-ray diffraction (XRD). The Cr, Mn, Fe, Co, and Ni atoms (256 in total) were randomly distributed in a proper concentration (20 at.% for each element) at the Wyckoff positions of the fcc lattice. The size of the simulation box was kept constant during the RMC simulations. The number of atomic configurations simultaneously considered in the EA algorithm was 32 [79].

In the current study, we followed the same procedure as described previously in Refs. [35, 36, 38]; the fixed simulation box size and small value of the largest permissible atom displacements (0.4 Å) play the role of constraints and stabilize the structural model. As a result, the final structural model does not deviate significantly from the selected crystallographic structure while it considers and can be used to describe both thermal and static disorders present in the alloy.

At each RMC iteration, the K-edge CA-EXAFS spectra $\chi(k)k^2$ were calculated over all Cr, Mn, Fe, Co, and Ni atoms in the constructed simulation box, and their Morlet WTs were compared with those of the experimental EXAFS spectra. The best agreement between the WTs of the experimental and calculated

CA-EXAFS spectra was used as a criterion for the model structure optimization. Comparing the spectra in the wavelet space allows one a better account of the small differences in scattering amplitudes for all types of 3d backscatters which are barely distinguishable not only in EXAFS but also in X-ray scattering experiments due to similarities in their scattering factors.

The WTs calculations were performed in the *k*-space range from 3.0 to 10.0 Å⁻¹ for Cr, from 3.0 to 12.0 Å⁻¹ for Fe, and from 3.0 to 10.5 Å⁻¹ for Mn, Co, and Ni; in the *R*-space, the calculations were done in the range from 1.2 to 6.0 Å for Cr, Fe, and Co, from 1.5 to 6.0 Å for Ni, and from 1.2 to 5.6 Å for Mn. Note that the ranges of the Cr, Mn, Fe, and Co EXAFS spectra are limited by the distance between their K absorption edges. The number of RMC iterations was 5000 to guarantee the convergence of the structural model; no significant improvements in the residuals were observed beyond this number. As a result of each RMC simulation, a set of final atomic coordinates was obtained, which was used to calculate the pair distribution functions (PDFs) $g(r)$, the mean interatomic distances $< R >$, the mean squared displacements (MSDs) for atoms of each type, and the mean square relative displacements (MSRDs) for each pair of atoms. To improve statistics, 10 sets of different (independent) starting structural models were considered for the final averaged PDFs.

During the RMC simulations, the CA-EXAFS spectra were calculated for atoms of each type (all principal components) using *ab initio* real-space multiple-scattering FEFF8.50L code [80, 81] including the MS effects up to the fourth order. More details about the simulations can be found in Ref. [38].

3 Results and discussion

3.1 Diffusion experiments

Several scenarios were considered by Gaertner et al. [57] to explain the appearance of kinks on the Arrhenius diagram presented in Fig. 2, among which a potential change of SRO that progressively formed at temperatures below the observed critical temperature of about 1150 K. It has been hypothesized that the random solid solution existing at high temperatures (HT state) starts featuring short-range ordering at the lower temperatures (LT state). However, it is not the atomic SRO that is relevant for vacancy-mediated diffusion in multi-component alloys (and which cannot be distinguished by EXAFS spectroscopy). One has to account for preferential atomic ordering around the vacancies, i.e., preferential element–vacancy bindings [82]. In a multi-component alloy, the tracer diffusion coefficient of an element *i* in the alloy can be presented as

$$D_i^{\star} = ga^2 f_i x_i (1 - \alpha_i) \exp\left(-\frac{\Delta G_{\mathrm{m}}}{RT}\right) \quad (1)$$

where *g* is the geometric factor (*g* = 1 for cubic crystals [53]), *a* is the lattice constant, f_i is the correlation factor, x_i is the concentration of the element *i* in the alloy (in at. fractions), ΔG_{m} is the free energy for migration, and RT has its usual meaning. The parameter α_i represents the Cowley–Warren SRO parameter [83, 84] of nearest-neighboring vacancy–element *i* pairs

$$\alpha_i = 1 - \frac{x_i^{v}}{x_i} \quad (2)$$

Here, x_i^{v} is the average concentration of the element *i* in the first coordination shell of the vacancy [82]. Equations (1) and (2) assume that self-diffusion in the alloy proceeds via nearest-neighbor jumps of vacancies, as is considered to be the case for diffusion in fcc metals and alloys [53].

For multicomponent systems, especially for multi-principal

element systems, it is important to consider that there exists a relatively broad distribution of vacancy formation energies depending on local configurations [49, 85, 86]. Potentially, this distribution influences the chemical species which are predominantly neighboring the vacancies at different temperatures, and in this way, the changes in the parameters α_i influence volume diffusion of the components.

According to the diffusion data [57], one may argue that vacancies are surrounded by different characteristic environments above and below the critical temperature interval of 1000–1150 K, and in our work, these temperature ranges are represented by the HT state annealed at 1373 K as compared to the LT state annealed at 993 K. Experimentally, after annealing under either HT or LT conditions the samples were cooled down relatively fast (quenching in cold water) preserving the atomic configurations around vacancies, thus allowing reliable EXAFS studies. Due to retarded diffusion in the fcc high-entropy alloys [45], this assumption seems to be reasonable.

3.2 EXAFS spectroscopy and qualitative frequency analysis

The local environment of principal components in the CrMnFeCoNi single crystal was explored down to the atomic scale by element-specific X-ray absorption spectroscopy at the K absorption edges of all 3d constituent elements. The normalized X-ray absorption spectra recorded at RT for the LT and HT annealed states are shown in Fig. 3. Each spectrum reflects the averaged over the probing volume local coordination of a particular type of atoms in the alloy. The shape and positions of EXAFS oscillations found above each absorption edge indicate a dominantly homogeneous short-range (local) environment of Cr, Mn, Fe, Co, and Ni absorbers in the fcc lattice with visibly suppressed oscillations found above the Cr and Ni K-edges for the LT annealed state (Fig. 3(a)). This suggests larger displacements of Cr and Ni atoms from their equilibrium positions in the crystallographic lattice or larger compositional disorder (e.g., variations in their local environment caused by noticeably diverse nearest backscatters or possible defects in the lattice) as compared to Fe, Co, and Mn constituents. In the HT annealed state, deviations in the amplitudes of EXAFS oscillations between all constituents are much less pronounced (Fig. 3(b)), with only visible changes for Cr. The possible contributions from the subsurface (down to several nm) oxidized atoms to the collected EXAFS spectra can be neglected in both cases due to the relatively large probing depth of FY detection mode (approx. 10–15 μm for the considered energy ranges).

The qualitative analysis of EXAFS oscillations done for each individual component in both states using the WTs is presented in Fig. 4. These WTs can be used for the visualization of similarities and differences in the local environment around each type of absorbers in the sample. All WTs demonstrate two distinct maxima of different relative intensities (at distances around 2.25 and 4.5 Å) representing the backscatters in the first and the second coordination shells, respectively. The visible deviations in the broadening of these maxima, which are more pronounced for the peak at 4.5 Å, can be associated with slight differences in the local coordination of a particular principal component. Interestingly, a clear blurring with a noticeably redistributed intensity over the peak associated with the second coordination shell was found solely for Ni atoms in the LT annealed state as well as some changes appeared for Mn in the HT annealed state. Other components demonstrate very similar WT patterns in both cases. Thus, it can be concluded that, except for Ni and Mn, the principal components of single crystalline CrMnFeCoNi under study are in very similar local environments caused by the constituting 3d elements at the atomic level, independently of the annealing temperature. However, some crucial differences are found for Ni atoms in the LT annealed state whereas some changes of similar origin were found for Mn in the HT annealed state, respectively.

Although WTs cannot be considered as real distribution functions of elements inside the multicomponent system, the qualitative result observed for Ni and Mn absorbers underlines the evident presence of characteristic peculiarities in the local environment of nickel and manganese atoms in the LT and HT annealed states of the studied HEA single crystal, correspondingly.

3.3 RMC simulations

To get a reliable three-dimensional (3D) structural model that represents the collected experimental data and accounts for static and dynamic lattice relaxations, we employed the RMC-based fitting procedure. The main peculiarities of atom distributions within the several first coordination shells of absorbers of each type can be described by a set of pair distribution functions $g(r)$ obtained using the RMC-based analysis applied to EXAFS data. Since the number of different local configurations around each principal component in five- (and more) component HEA systems is on the order of billions whereas only a limited number of initial configurations can be considered during the simulations, the outcomes of the fit underline the most significant statistically averaged quantities [38].

An example of the initial configuration of atoms used in the simulation box during the RMC analysis and its final modifications due to lattice relaxations for the LT and HT annealed states is shown in Fig. 5. The particular structural model
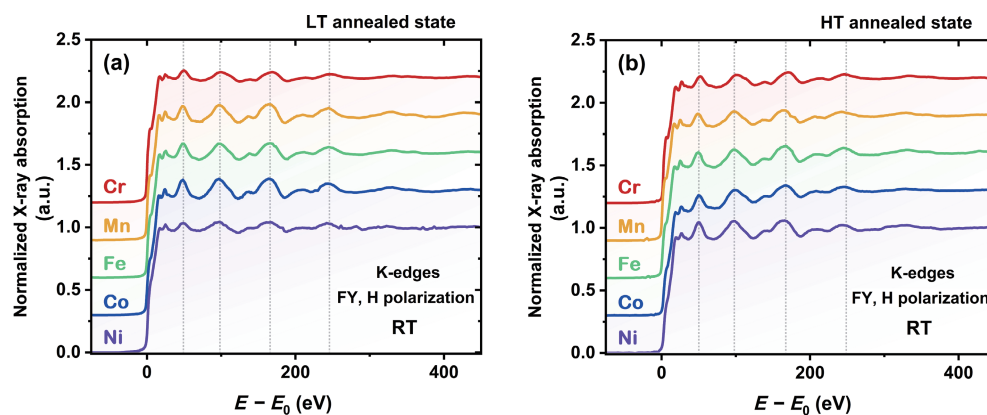
Figure 3 X-ray absorption spectra of the CrMnFeCoNi single crystal in (a) the LT and (b) HT annealed states recorded at the K absorption edges of Cr (E_0 = 5988.5 eV), Mn (E_0 = 6539 eV), Fe (E_0 = 7112 eV), Co (E_0 = 7708.5 eV), and Ni (E_0 = 8333 eV) at RT using FY. E_0 was determined as the energy corresponding to the first maximum of the first derivative of each particular spectrum. The spectra are normalized to unity and shifted vertically for clarity.
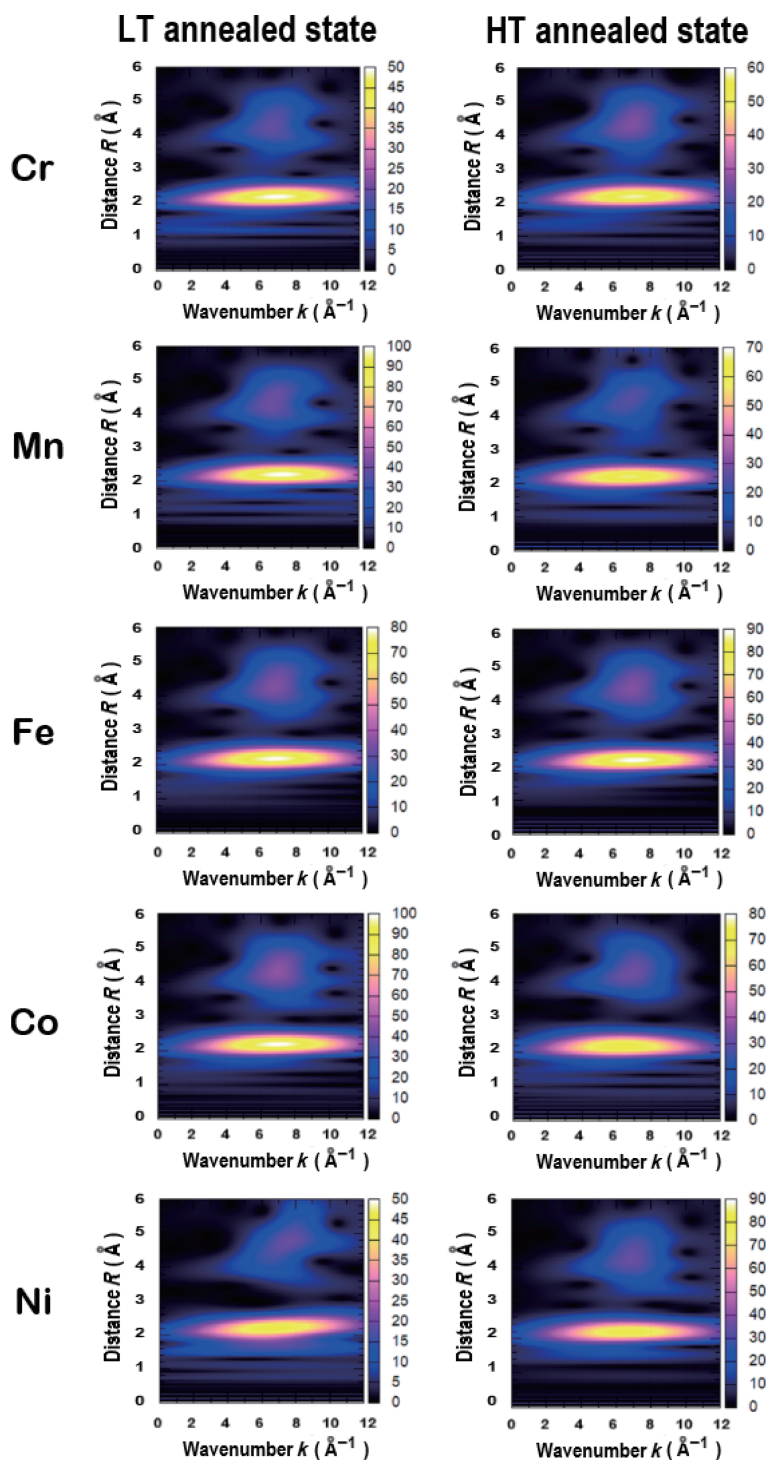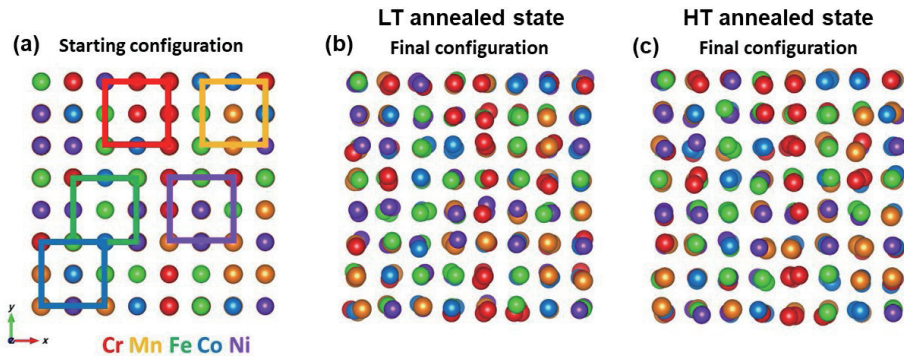
Figure 4 WTs for the CrMnFeCoNi single crystal in the LT (left panels) and HT (right panels) annealed states at 300 K extracted from the K-edge EXAFS spectra $\chi(k)k^2$ of Cr, Mn, Fe, Co, and Ni, correspondingly.

was simultaneously fitted to EXAFS spectra independently collected at five K absorption edges to find the coordinates of all relaxed atoms in the constructed supercell. The obtained atomic coordinates were further used to calculate the total and partial component-specific PDFs.

The experimental and RMC-fitted CA-EXAFS spectra together with their FTs are shown in Fig. 6. A good reproducibility of the experimental EXAFS data by RMC-fitted ones is found in both k and R spaces at all considered K-edges, including the visible peculiarities in FTs up to 6 Å. This suggests that the final structural model based on atoms randomly distributed over the supercell is self-consistent and reproduces the experimental data with reasonable accuracy. Moreover, in the special case of the fcc

structure, where the first peak in the FTs of the experimental EXAFS spectra is well isolated and located between 1.0 and 3.0 Å (Fig. 6), eligible accuracy of any further quantitative estimations related to the nearest-neighbors around absorbers of each type is also assured. Thus, the extracted total PDFs represent the most essential details of the nearest-neighbor arrangements in the first coordination shell of the corresponding 3d absorber.

This approach allows performing a reliable analysis of the available experimental EXAFS data in the most unbiased manner without any additional assumptions about possible interrelations between fitted parameters and reconstructing the local environment in the first five coordination shells around each type of the 3d absorbers (distances up to ~ 6.0 Å). The displacements of

Figure 5 Examples of (a) starting (initial) and ((b) and (c)) final atom configurations (simulation boxes) used in the RMC simulations for simultaneous fit to the EXAFS spectra of the CrMnFeCoNi single crystal at five K absorption edges (Cr, Mn, Fe, Co, and Ni) in (b) the LT and (c) HT annealed states at 300 K. The initial simulation box (a) was randomly filled with atoms according to the film composition; periodic boundary conditions were applied to minimize the influence of surface effects. Colour scheme: Cr (red), Mn (gold/orange), Fe (light green), Co (blue), and Ni (violet). The top views of the simulation boxes are shown along the *z*-direction in chosen *xyz* coordinates as depicted in (a). The schematic border of the fcc unit cells around each principal component is displayed in the figure related to the starting configuration.
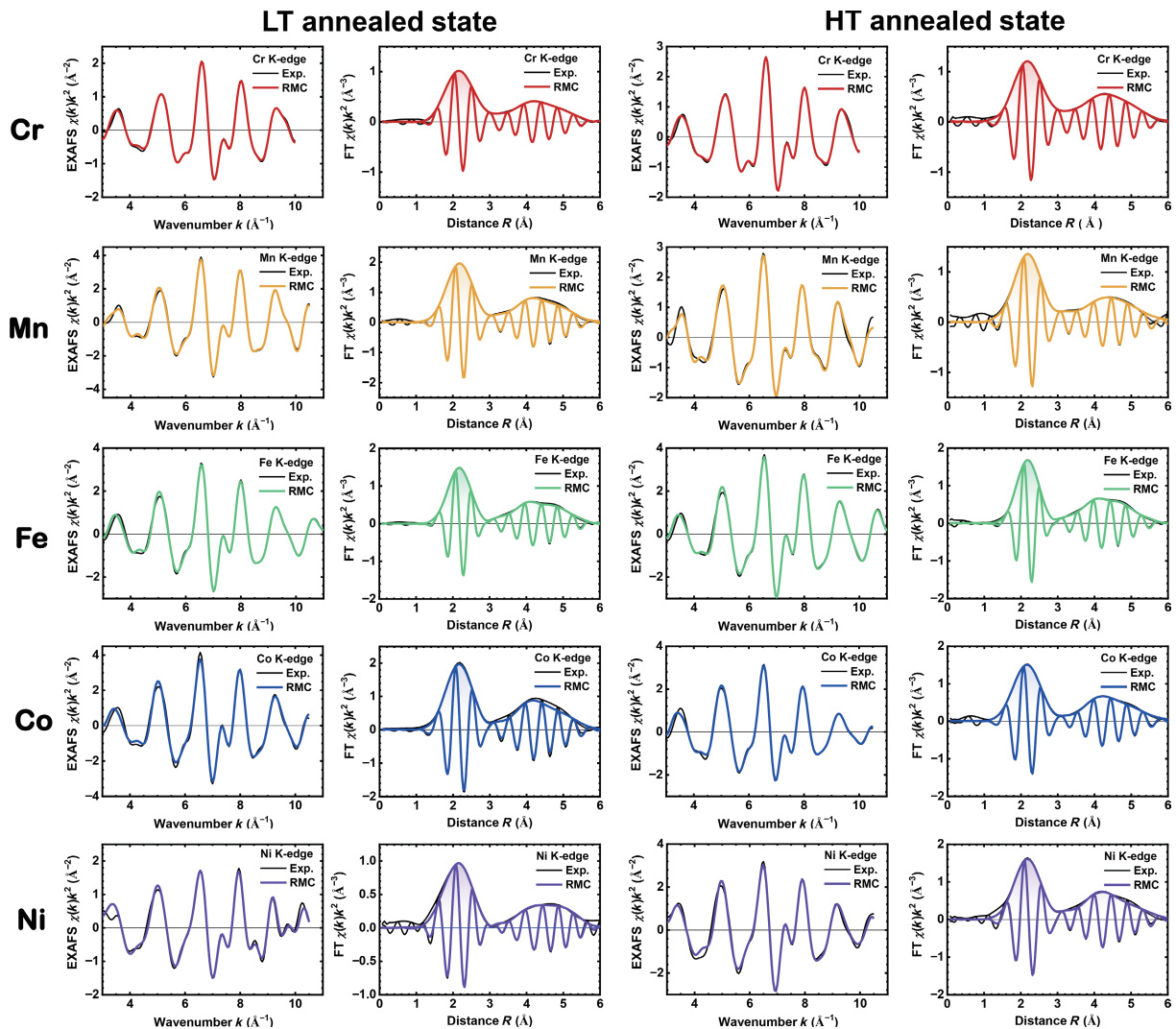

Figure 6 Experimental (black lines) and RMC-calculated (colored lines) K-edge EXAFS spectra $\chi(k)k^2$ of Cr, Mn, Fe, Co, and Ni, as well as their FTs for the CrMnFeCoNi single crystal in the LT (two left panels) and HT (two right panels) annealed states at 300 K.

atoms present in the final configurations account for both thermal (dynamic) and structural (radial and angular) disorders.

It is worth noting that an important question about possible atomic short-range ordering effects expected in the Cantor alloy cannot be properly addressed by the RMC-based analysis due to similarities of scattering amplitudes for all 3d principal components that act as backscatters (see Fig. 7). This creates an uncertainty in distinguishing between 3d constituents located in

the first (and other) coordination shell(s) of absorbers of each type and does not allow strong discussions about the distribution of individual components over the coordination shells of a particular absorber narrowing the conclusions. However, it does not influence the averaged values of interatomic distances and component-dependent structural relaxations extracted from the total PDFs that will be discussed further. The same problem exists for the anomalous scattering experiments, where the recorded
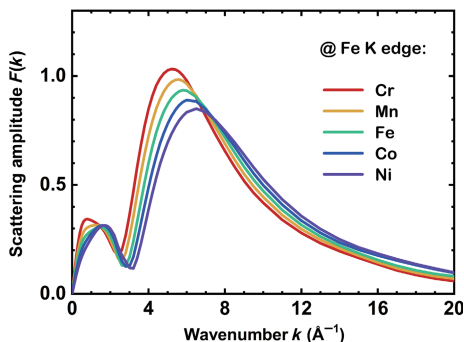
Figure 7 Illustration of differences in the scattering amplitudes employed in the RMC calculations and associated with neighboring 3d elements acting as backscatters around Fe absorbers in the considered HEA.
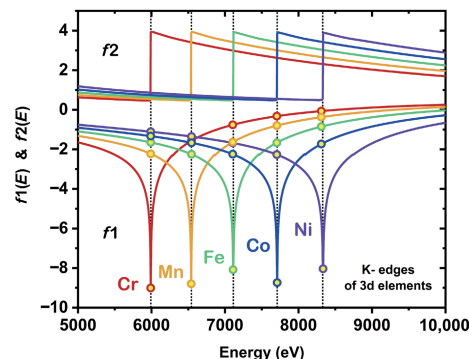

Figure 8 Scattering amplitudes $f1(E)$ and $f2(E)$ for pure Cr, Mn, Fe, Co, and Ni within the energy range covering the K absorption edges of corresponding 3d elements [87].

signal is dependent on real, $f1(E)$, and imaginary, $f2(E)$, parts of the X-ray scattering factors shown in Fig. 8. At each absorption edge, only resonant atoms (the particular absorbers) exhibit $f1(E)$ values which significantly differ from those of other components while all non-resonant atoms have very similar values of $f1(E)$.

A set of total PDFs calculated from the atomic coordinates of the final structural models for the LT and HT annealed states is shown in Fig. 9. Each of these PDFs is a component-specific projection of the three-dimensional structure of the studied single

crystal over a radial distance relative to the chosen absorbing atom and describes the configuration-averaged local environment around a particular absorber. For each state, the principal components demonstrate total PDFs with the same number and positions of peaks within the first five coordination shells corresponding to a distribution of all atoms over the fcc lattice sites confirming the single-phase of the single crystalline HEA within a sensitivity of the applied RMC method.
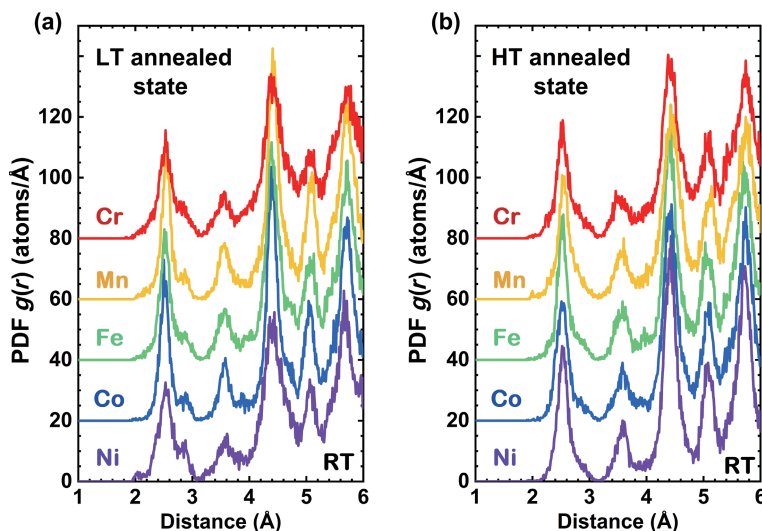
Figure 9 Total pair distribution functions $g(r)$ for the CrMnFeCoNi single crystal in (a) the LT and (b) HT annealed states at 300 K extracted from the K-edge EXAFS spectra $\chi(k)k^2$ of Cr, Mn, Fe, Co, and Ni using the RMC method. Curves are shifted vertically for clarity.
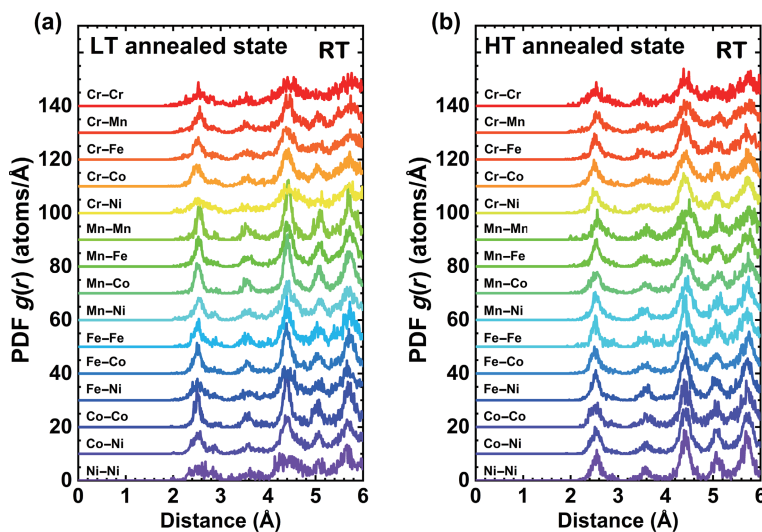
Figure 10 Partial pair distribution functions $g(r)$ for the CrMnFeCoNi single crystal in (a) the LT and (b) HT annealed states at 300 K extracted from the K-edge EXAFS spectra $\chi(k)k^2$ of Cr, Mn, Fe, Co, and Ni using the RMC method. Curves are shifted vertically for clarity. In (a) the largest broadening of PDFs containing Cr and Ni is well-visible, especially for Cr–Cr, Cr–Ni, Fe–Ni, and Ni–Ni pairs; in (b) some broadening of PDFs is visible for Cr–Cr, Cr–Mn, and Mn–Mn pairs.

Nevertheless, clear differences between the two studied states were found: The first peak in total PDFs for the LT annealed state has a visible double structure (it exhibits a visible side peak towards larger distances), which is the most pronounced for Ni atoms in terms of the relative intensity and the size of splitting, while the HT annealed state demonstrates much more uniform and more narrow distribution $g(r)$ for all components. In general, more narrow peaks of PDFs indicate that the positions of particular atoms in the simulation box have smaller deviations from their equilibrium positions assumed for the ideal lattice.

The MSDs for all components calculated directly from the coordinates of atoms according to the final configurations are shown in Table 1. For both states, the MSDs values of Cr, Fe, Co, and Ni components are larger as compared to the pure bulk metals (see Table 1, last column), but smaller (except for Ni) as compared to the single-phase nanocrystalline Mn-rich $Cr_{20}Mn_{26}Fe_{18}Co_{19}Ni_{17}$ film [36]. This suggests that despite both states exhibiting larger disorders for the components in the HEA single crystal as compared with the bulk metals due to their heterogeneity at the atomic level, the studied states of the HEA single crystal are much more ordered in all shells than the nanocrystalline $Cr_{20}Mn_{26}Fe_{18}Co_{19}Ni_{17}$ film. The only exception was found for the Ni component in the LT annealed state (MSD is 0.054 Å²) which has almost the same degree of disorder as in the abovementioned film (MSD is 0.053 Å² [36]).

A fully surprising result was found for the Mn component: Although both states demonstrate the expected smaller MSDs of Mn for the HEA single crystal as compared to α-Mn with four crystallographically inequivalent Mn sites [88], for the HT annealed state the enlarged MSD of Mn (0.042 Å²) was found, which is even larger than in the Mn-rich nanocrystalline $Cr_{20}Mn_{26}Fe_{18}Co_{19}Ni_{17}$ film (0.029 Å² [36]). Taking into account the outcomes of WTs found for both annealed states (Fig. 4), we can speak about the anomalies in the short-range local environment evidenced in the enhanced Mn displacements after the homogenization treatment, i.e., annealing in HT state, whereas Ni atoms become demonstrating larger displacements in the LT annealed state.

The statistically averaged mean interatomic distances $< R >$ and the MSRDs (Table 1) were numerically obtained as the first and second moments of the total PDFs for atoms of each type in states before and after the final annealing. The statistically averaged distances $< R >$ are in the range of 2.56–2.57 Å for all components in both states without showing any visible preferences; however, these values are a bit larger than previously reported in Refs. [35, 36, 38] for other fcc HEAs and calculated for the foils of hcp/fcc Co (2.51/2.52 Å) and fcc Ni (2.50 Å) [38]. At the same time, the LT and HT annealed states exhibit stronger differences in MSRDs,

showing the same trend as was found for the MSD values. In the LT annealed state, the MSRD value related to Cr is the largest one (0.046 Å²), while the MSRD value related to Ni atoms is the second largest one (0.042 Å²) and the MSRDs extracted from the total PDFs related to Mn, Fe, and Co absorbers demonstrate the intermediate values in the range of 0.028–0.033 Å². For the HT annealed state, the MSRD value related to Cr is the largest one (0.038 Å²) as well, while the second largest MSRD value was found for Mn (0.032 Å²). Other components (Fe, Co, and Ni) demonstrate the intermediate MSRD values in the range of 0.024–0.028 Å². Thus, according to MSD and MRSD values found for Cr, Ni, and Mn, these components demonstrate a larger degree of the compositional disorder determined by peculiarities in their local environments in the corresponding states of the studied HEA single crystal, but the reasons for such a disorder can be different.

A larger local static disorder around Cr and Mn atoms compared to that around Fe, Co, and Ni has been also found from EXAFS data in a series of equiatomic alloys CrCoNi, MnFeCoNi, CrFeCoNi, and CrMnFeCoNi [33]. Note that a simple Gaussian model with several constraints, required to limit the total number of free parameters, has been employed [33]. While the absolute values of the MSRD factors found in Ref. [33] are significantly lower than our results, the main qualitative tendency is similar. Besides, the density-functional theory calculations have been used to correlate the observed local lattice distortions with the electronic structure of the alloys: The authors propose that while different factors can affect the displacements of atoms, charge transfer between neighboring elements is their major cause [33, 89].

The total PDFs (Fig. 9) and the related parameters presented in Table 1 should be considered as the most reliable outcomes of the RMC simulations representing the structural model of the system at the atomic scale. At the same time, the availability of atomic coordinates in the final atom configurations allows one to calculate the partial PDFs (Fig. 10) as well. Their detailed analysis and interpretation should however be done with care, taking into account a possible ambiguity of such decomposition due to the similarities of the backscattering amplitudes of the constituting 3d elements (see Fig. 7). The extracted partial PDFs (Fig. 10) reveal a much more complex structure depending on the particular pairs of atoms. For the LT annealed state, all pairs containing Cr and Ni demonstrate a reduced intensity, enlarged broadening, or the double structure of the first peak related to the first coordination shell; the largest broadening of PDFs occurs for the Cr–Cr, Cr–Ni, Fe–Ni, and Ni–Ni pairs. In the HT annealed state only the PDFs for Cr–Cr, Cr–Mn, and Mn–Mn pairs are visibly different from others. Note that despite of the random distribution of metal atoms in the simulation box during RMC-based analysis, the shapes obtained for partial PDFs can be clearly distinguished

Table 1 Component-dependent structural parameters (MSD, MSRD, and $< R >$) extracted from the total PDFs of CrMnFeCoNi single crystal in the LT and HT annealed states at 300 K. The error bars for the MSD and MSRD values are about ±0.003 Å² in all cases. The MSD values extracted from PDFs of Cr, Mn, Fe, Co, and Ni pure metals are given for comparison; the RMC analysis for pure elements was done within the same approach as for the considered HEA[a]

	LT annealed state			HT annealed state			Pure metals [36, 38]
	MSD (Å²)	MSD and MSRD@RT	MSRD (Å²)	MSD (Å²)	MSD and MSRD@RT	MSRD (Å²)	MSD (Å²)
Cr	0.062	The largest	0.046	0.053	The largest	0.038	0.017 (bcc)
Mn	0.026		0.029	0.042	2nd largest	0.032	0.048 (α-Mn)
Fe	0.035	Intermediate values	0.033	0.031		0.028	0.014 (bcc)
Co	0.026		0.028	0.030	Intermediate values	0.027	0.017/0.023 (hcp/fcc)
Ni	0.054	2nd largest	0.042	0.025		0.024	0.017 (fcc)

[a]The statistically averaged distances for all components are $<R>$ = 2.56–2.57 Å (±0.02 Å).

between more ordered and significantly broadened ones, reproducing the tendency found for the total PDFs. Thus, in general, either total or partial PDFs point out that the HT annealed state is much more ordered as compared with the LT annealed one, and some peculiarities are present for Cr, Ni, and Mn depending on the considered state.

The tendency of having the largest uncertainties and variations in distances to the nearest neighbors around Cr absorbers valid for the CrMnFeCoNi single crystal studied in this work is in agreement with the previous results obtained for the $Al_{0.3}$-CrFeCoNi [35], macroscopic flakes of equiatomic CrMnFeCoNi [38], bulk CrMnFeCoNi [33], and the nanocrystalline Mn-rich $Cr_{20}Mn_{26}Fe_{18}Co_{19}Ni_{17}$ film [36].

The EXAFS spectroscopy data demonstrate that there exist characteristic differences between the LT and HT states concerning disorder anomalies in the local environments of Ni and Mn atoms. Meantime, the vacancy concentrations estimated for these states from the data on vacancy formation energies after Sugita et al. [85] reported the values of 6×10^{-7} and 3×10^{-9} in at. fractions at 1373 K (HT state) and 993 K (LT state), respectively. This concentration of vacancies is too low to be included in the structural model we used for the RMS simulations and is also not detectable in the EXAFS spectra. However, considering the vacancy-mediated origin of the elemental diffusion in multi-component alloys it might be possible to assign these anomalies to the dominance of Mn- and Ni-enriched neighborhood of thermal vacancies in the HT and LT states, respectively.

A detailed explanation of the Arrhenius diagram, including the precise values of the characteristic temperatures and self-diffusion coefficients from an atomistic point of view, is beyond the scope of this work, as much deeper experimental studies or density functional theory (DFT) calculations and rigorous kinetic modelling are required. Nevertheless, based on the current element-specific EXAFS spectroscopy outcomes, a number of correlations with the results found earlier in Ref. [57] from the tracer diffusion experiments can be highlighted.

First, one has to notice that the HT state discussed in the present work corresponds to typical temperature intervals of the vast majority of the experimental diffusion studies on CrMnFeCoNi HEA published so far [44, 46–49, 55, 90, 91]. In all those investigations, the Arrhenius-type temperature dependencies were reported. The study by Gaertner et al. [57] is to the best of our knowledge the only one which was extended to include the low-temperature states about the predicted thermodynamic limits of stability of the fcc solid solution phase, see Refs. [42, 92]. As a result, characteristic deviations (kinks) in the temperature dependencies of the measured tracer diffusivities were observed [57].

Second, there is an exciting correlation between the two fundamentally independent datasets, i.e. the tracer diffusion data [57] and the present EXAFS spectroscopy data, related to the HT or LT states regarding the disorder anomalies found for specific components and their diffusion rates relative to other elements. At the high temperatures represented by the HT state, Mn has the largest diffusion rate D^* among all constituents which correlates with the assumed vacancy availability in the vicinity of Mn atoms. That in turn can be explained by an increased concentration of Mn atoms as nearest-neighbors of vacancies despite the random solid solution is still preserved on average. At lower temperatures the situation is different, and Ni progressively becomes the fastest element with the largest increase of D^* [57]. Remarkably, the LT state prepared by the long-term annealing at 993 K reveals the pronounced disorder anomaly solely for Ni, while the Mn signal loses completely such a signature. This spectacular correlation is the most important finding of the present study.

Third, the kinks in the temperature dependencies of the

elemental self-diffusion coefficients for Co & Ni and for Cr & Fe appear in notably spaced temperature ranges. The diffusion behaviors of Co and Ni, as well as of Cr and Fe, were frequently reported to be quite similar in the CrMnFeCoNi alloy [44, 47]. This correlates with the experimentally established tendency in the component-dependent structure relaxations for these types of atoms in the family of Cantor alloys [35, 36, 38]. In fact, it was pointed out that both Co and Ni demonstrate smaller structural relaxations and, accordingly, experience less stress while accommodating the fcc crystallographic lattice of HEAs as compared to Cr and Fe, which initially have bcc lattices in their equilibrium bulk form as pure elements. For Mn, the situation is more complicated due to its initial α-Mn cubic structure. Earlier, the DFT calculations predicted the smallest value of mean-squared atomic distortions for Ni and the largest value for Cr atoms, while Co, Fe, and Mn reveal the values in between these two extremes [28, 93]. This general tendency is also valid for the single crystalline CrMnFeCoNi alloy under study with the only exception for Ni in the LT state. The importance of the local atomically-resolved elastic distortions for the diffusion analysis in HEAs was previously recognized in the recent work of Dash et al. [45], and our EXAFS data support these findings by detecting the changes in the compositional disorder in HT and LT states, despite MSDs do not show any straightforward relation with the relative diffusivities.

In such a way, the EXAFS spectroscopy in conjunction with the RMC-based analysis provides new atomistic insights and corroborates a view that disorder anomalies (most likely vacancy-induced) existing in the local environment influence the tracer diffusion rates of the alloying elements resulting in discontinuities in the Arrhenius-type temperature dependencies.

4   Conclusions

The advanced structural characterization of the single crystalline CrMnFeCoNi high-entropy alloy performed with the use of multi-edge EXAFS spectroscopy in conjunction with RMC simulations has allowed us to probe the details of element-specific local environments in two characteristic annealing temperature ranges determined earlier from the tracer diffusion measurements. Two distinct states—the HT and LT ones—intentionally prepared by annealing above (at 1373 K) and below (at 993 K) the critical temperature interval, respectively, were found to be single-phase at the atomic scale with the largest local compositional disorder within the first coordination shell for Cr atoms as in other forms of the Cantor alloy (bulk, macroscopic flakes, or the nanocrystalline film) or in the modified Cantor alloy with aluminum.

The component-dependent PDFs revealed from the RT EXAFS spectroscopy data collected at the K absorption edges of each principal component suggest that the LT state in general is more disordered as compared to the HT one confirming the sensitivity of atomic configurations to annealing conditions despite the initial homogenization was done at high temperature. The increased disorder found for the LT state is consistent with the phase decomposition tendency known for the lower annealing temperatures. The qualitative outcomes of WTs considered together with the quantitative details of PDFs point out the peculiarities in the Ni and Mn local environments for the LT and HT annealed states, respectively, while all other principal components demonstrate a very similar local environment formed by 3d constituents independently on the annealing temperature. The observed disorder anomalies in the Ni and Mn local environments were indirectly associated with an increased probability of the presence of vacancies in the vicinity of these particular components.

The characteristic differences found for the LT and HT annealed states with respect to Ni and Mn atoms were correlated with the earlier observed changes in the relative self-diffusion rates of the same elements and along with the component-dependent atomic relaxations provide important atomistic insights into the discontinuities in the Arrhenius-type temperature dependencies found by the tracer diffusion measurements for the single crystalline HEA system under study.

Acknowledgements

References

[1] Cantor, B.; Chang, I. T. H.; Knight, P.; Vincent, A. J. B. Microstructural development in equiatomic multicomponent alloys. *Mater. Sci. Eng. A* **2004**, *375–377*, 213–218

[2] Yeh, J. W.; Chen, S. K.; Lin, S. J.; Gan, J. Y.; Chin, T. S.; Shun, T. T.; Tsau, C. H.; Chang, S. Y. Nanostructured high-entropy alloys with multiple principal elements: Novel alloy design concepts and outcomes. *Adv. Eng. Mater.* **2004**, *6*, 299–303.

[3] Kao, Y. F.; Chen, S. K.; Sheu, J. H.; Lin, J. T.; Lin, W. E.; Yeh, J. W.; Lin, S. J.; Liou, T. H.; Wang, C. W. Hydrogen storage properties of multi-principal-component CoFeMnTi$_x$V$_y$Zr$_z$ alloys. *Int. J. Hyd. Energy* **2010**, *35*, 9046–9059.

[4] Zaddach, A. J.; Niu, C.; Koch, C. C.; Irving, D. L. Mechanical properties and stacking fault energies of NiFeCrCoMn high-entropy alloy. *JOM* **2013**, *65*, 1780–1789.

[5] Gludovatz, B.; Hohenwarter, A.; Catoor, D.; Chang, E. H.; George, E. P.; Ritchie, R. O. A fracture-resistant high-entropy alloy for cryogenic applications. *Science* **2014**, *345*, 1153–1158.

[6] Schuh, B.; Mendez-Martin, F.; Völker, B.; George, E. P.; Clemens, H.; Pippan, R.; Hohenwarter, A. Mechanical properties, microstructure and thermal stability of a nanocrystalline CoCrFeMnNi high-entropy alloy after severe plastic deformation. *Acta Mater.* **2015**, *96*, 258–268.

[7] Huang, S.; Li, W.; Lu, S.; Tian, F. Y.; Shen, J.; Holmström, E.; Vitos, L. Temperature dependent stacking fault energy of FeCrCoNiMn high entropy alloy. *Scr. Mater.* **2015**, *108*, 44–47.

[8] Varvenne, C.; Luque, A.; Curtin, W. A. Theory of strengthening in fcc high entropy alloys. *Acta Mater.* **2016**, *118*, 164–176.

[9] Sahlberg, M.; Karlsson, D.; Zlotea, C.; Jansson, U. Superior hydrogen storage in high entropy alloys. *Sci. Rep.* **2016**, *6*, 36770.

[10] Wang, B. F.; Fu, A.; Huang, X. X.; Liu, B.; Liu, Y.; Li, Z. Z.; Zan, X. Mechanical properties and microstructure of the CoCrFeMnNi high entropy alloy under high strain rate compression. *J. Mater. Eng. Perform.* **2016**, *25*, 2985–2992.

[11] Zhang, Y. W.; Zhao, S. J.; Weber, W. J.; Nordlund, K.; Granberg, F.; Djurabekova, F. Atomic-level heterogeneity and defect dynamics in concentrated solid-solution alloys. *Curr. Opin. Solid State Mater. Sci.* **2017**, *21*, 221–237.

[12] Ahmad, A. S.; Su, Y.; Liu, S. Y.; Ståhl, K.; Wu, Y. D.; Hui, X. D.; Ruett, U.; Gutowski, O.; Glazyrin, K.; Liermann, H. P. et al. Structural stability of high entropy alloys under pressure and temperature. *J. Appl. Phys.* **2017**, *121*, 235901.

[13] Luo, H.; Li, Z. M.; Mingers, A. M.; Raabe, D. Corrosion behavior of an equiatomic CoCrFeMnNi high-entropy alloy compared with 304 stainless steel in sulfuric acid solution. *Corros. Sci.* **2018**, *134*, 131–139.

[14] Shi, Y. Z.; Collins, L.; Feng, R.; Zhang, C.; Balke, N.; Liaw, P. K.; Yang, B. Homogenization of Al$_x$CoCrFeNi high-entropy alloys with improved corrosion resistance. *Corros. Sci.* **2018**, *133*, 120–131.

[15] Löffler, T.; Meyer, H.; Savan, A.; Wilde, P.; Garzón Manjón, A.; Chen, Y. T.; Ventosa, E.; Scheu, C.; Ludwig, A.; Schuhmann, W. Discovery of a multinary noble metal-free oxygen reduction catalyst. *Adv. Energy Mater.* **2018**, *8*, 1802269.

[16] Kong, K.; Hyun, J.; Kim, Y.; Kim, W.; Kim, D. Nanoporous structure synthesized by selective phase dissolution of AlCoCrFeNi high entropy alloy and its electrochemical properties as supercapacitor electrode. *J. Power Sources* **2019**, *437*, 226927.

[17] Xu, X.; Du, Y. K.; Wang, C. H.; Guo, Y.; Zou, J. W.; Zhou, K.; Zeng, Z.; Liu, Y. Y.; Li, L. Q. High-entropy alloy nanoparticles on aligned electronspun carbon nanofibers for supercapacitors. *J. Alloys Compd.* **2020**, *822*, 153642.

[18] Fang, G.; Gao, J. J.; Lv, J.; Jia, H. L.; Li, H. L.; Liu, W. H.; Xie, G. Q.; Chen, Z. H.; Huang, Y.; Yuan, Q. H. et al. Multi-component nanoporous alloy/(oxy)hydroxide for bifunctional oxygen electrocatalysis and rechargeable Zn-air batteries. *Appl. Catal. B: Environ.* **2020**, *268*, 118431.

[19] Pedersen, J. K.; Batchelor, T. A. A.; Bagger, A.; Rossmeisl, J. High-entropy alloys as catalysts for the CO$_2$ and CO reduction reactions. *ACS Catal.* **2020**, *10*, 2169–2176.

[20] Yao, Y. G.; Huang, Z. N.; Li, T. Y.; Wang, H.; Liu, Y. F.; Stein, H. S.; Mao, Y. M.; Gao, J. L.; Jiao, M. L.; Dong, Q. et al. High-throughput, combinatorial synthesis of multimetallic nanoclusters. *Proc. Natl. Acad. Sci. USA* **2020**, *117*, 6316–6322.

[21] Pickering, E. J.; Carruthers, A. W.; Barron, P. J.; Middleburgh, S. C.; Armstrong, D. E. J.; Gandy, A. S. High-entropy alloys for advanced nuclear applications. *Entropy* **2021**, *23*, 98.

[22] Zhu, M.; Zhao, B. Z.; Yuan, Y. F.; Guo, S. Y.; Wei, G. Y. Study on corrosion behavior and mechanism of CoCrFeMnNi HEA interfered by AC current in simulated alkaline soil environment. *J. Electroanal. Chem.* **2021**, *882*, 115026.

[23] Ma, Y. J.; Ma, Y.; Wang, Q. S.; Schweidler, S.; Botros, M.; Fu, T. T.; Hahn, H.; Brezesinski, T.; Breitung, B. High-entropy energy materials: Challenges and new opportunities. *Energy Environ. Sci.* **2021**, *14*, 2883–2905.

[24] Guo, S.; Ng, C.; Lu, J.; Liu, C. T. Effect of valence electron concentration on stability of fcc or bcc phase in high entropy alloys. *J. Appl. Phys.* **2011**, *109*, 103505.

[25] Čížek, L.; Kratochvíl, P.; Smola, B. Solid solution hardening of copper crystals. *J. Mater. Sci.* **1974**, *9*, 1517–1520.

[26] Gypen, L. A.; Deruyttere, A. Multi-component solid solution hardening. *J. Mater. Sci.* **1977**, *12*, 1028–1033.

[27] Ma, D. C.; Grabowski, B.; Körmann, F.; Neugebauer, J.; Raabe, D. *Ab initio* thermodynamics of the CoCrFeMnNi high entropy alloy: Importance of entropy contributions beyond the configurational one. *Acta Mater.* **2015**, *100*, 90–97

[28] Okamoto, N. L.; Yuge, K.; Tanaka, K.; Inui, H.; George, E. P. Atomic displacement in the CrMnFeCoNi high-entropy alloy-A scaling factor to predict solid solution strengthening. *AIP Adv.* **2016**, *6*, 125008.

[29] Tong, Y.; Velisa, G.; Yang, T.; Jin, K.; Lu, C.; Bei, H.; Ko, J. Y. P.; Pagan, D. C.; Huang, R.; Zhang, Y. et al. Probing local lattice distortion in medium- and high-entropy alloys. 2017, arXiv: 1707.07745. arXiv.org e-Print archive. https://doi.org/10.48550/arXiv.1707.077459 (accessed Apr 1, 2022).

[30] Zhang, F. X.; Tong, Y.; Jin, K.; Bei, H. B.; Weber, W. J.; Huq, A.; Lanzirotti, A.; Newville, M.; Pagan, D. C.; Ko, J. Y. P. et al. Chemical complexity induced local structural distortion in NiCoFeMnCr high-entropy alloy. *Mater. Res. Lett.* **2018**, *6*, 450–455.

[31] Ding, Q. Q.; Zhang, Y.; Chen, X.; Fu, X. Q.; Chen, D. K.; Chen, S. J.; Gu, L.; Wei, F.; Bei, H. B.; Gao, Y. F. et al. Tuning element distribution, structure and properties by composition in high-entropy alloys. *Nature* **2019**, *574*, 223–227.

[32] Cantor, B. Multicomponent high-entropy Cantor alloys. *Prog. Mater. Sci.* **2021**, *120*, 100754.

[33] Oh, H. S.; Odbadrakh, K.; Ikeda, Y.; Mu, S.; Körmann, F.; Sun, C. J.; Ahn, H. S.; Yoon, K. N.; Ma, D. C.; Tasan, C. C. et al. Element-resolved local lattice distortion in complex concentrated alloys: An observable signature of electronic effects. *Acta Mater.* **2021**, *216*, 117135.

[34] Billington, D.; James, A. D. N.; Harris-Lee, E. I.; Lagos, D. A.; O'Neill, D.; Tsuda, N.; Toyoki, K.; Kotani, Y.; Nakamura, T.; Bei, H. et al. Bulk and element-specific magnetism of medium-entropy and high-entropy Cantor–Wu alloys. *Phys. Rev. B* **2020**, *102*, 174405.

[35] Smekhova, A.; Kuzmin, A.; Siemensmeyer, K.; Luo, C.; Chen, K.; Radu, F.; Weschke, E.; Reinholz, U.; Buzanich, A. G.; Yusenko, K. V. Al-driven peculiarities of local coordination and magnetic properties in single-phase Al$_x$-CrFeCoNi high-entropy alloys. *Nano Res.* **2022**, *15*, 4845–4858.

[36] Smekhova, A.; Kuzmin, A.; Siemensmeyer, K.; Luo, C.; Taylor, J.; Thakur, S.; Radu, F.; Weschke, E.; Buzanich, A. G.; Xiao, B. et al. Local structure and magnetic properties of a nanocrystalline Mn-rich Cantor alloy thin film down to the atomic scale. *Nano Res.* **2023**, *16*, 5626–5639.

[37] Oh, H. S.; Ma, D. C.; Leyson, G. P.; Grabowski, B.; Park, E. S.; Körmann, F.; Raabe, D. Lattice distortions in the FeCoNiCrMn high entropy alloy studied by theory and experiment. *Entropy* **2016**, *18*, 321.

[38] Smekhova, A.; Kuzmin, A.; Siemensmeyer, K.; Abrudan, R.; Reinholz, U.; Buzanich, A. G.; Schneider, M.; Laplanche, G.; Yusenko, K. V. Inner relaxations in equiatomic single-phase high-entropy Cantor alloy. *J. Alloys Compd.* **2022**, *920*, 165999.

[39] Wilson, J. A.; Moore, C.; Goddard, D. T.; Middleburgh, S. C. Assessing the high concentration of vacancies in refractory high entropy alloys. *Materialia* **2023**, *28*, 101764.

[40] Zhang, R. P.; Zhao, S. T.; Ding, J.; Chong, Y.; Jia, T.; Ophus, C.; Asta, M.; Ritchie, R. O.; Minor, A. M. Short-range order and its impact on the CrCoNi medium-entropy alloy. *Nature* **2020**, *581*, 283–287.

[41] He, Q. F.; Tang, P. H.; Chen, H. A.; Lan, S.; Wang, J. G.; Luan, J. H.; Du, M.; Liu, Y.; Liu, C. T.; Pao, C. W. et al. Understanding chemical short-range ordering/demixing coupled with lattice distortion in solid solution high entropy alloys. *Acta Mater.* **2021**, *216*, 117140.

[42] Bracq, G.; Laurent-Brocq, M.; Perrière, L.; Pirès, R.; Joubert, J. M.; Guillot, I. The fcc solid solution stability in the Co-Cr-Fe-Mn-Ni multi-component system. *Acta Mater.* **2017**, *128*, 327–336.

[43] Otto, F.; Dlouhý, A.; Pradeep, K. G.; Kuběnová, M.; Raabe, D.; Eggeler, G.; George, E. P. Decomposition of the single-phase high-entropy alloy CrMnFeCoNi after prolonged anneals at intermediate temperatures. *Acta Mater.* **2016**, *112*, 40–52.

[44] Tsai, K. Y.; Tsai, M. H.; Yeh, J. W. Sluggish diffusion in Co-Cr-Fe-Mn-Ni high-entropy alloys. *Acta Mater.* **2013**, *61*, 4887–4897.

[45] Dash, A.; Paul, A.; Sen, S.; Divinski, S.; Kundin, J.; Steinbach, I.; Grabowski, B.; Zhang, X. Recent advances in understanding diffusion in multiprincipal element systems. *Ann. Rev. Mater. Res.* **2022**, *52*, 383–409.

[46] Vaidya, M.; Trubel, S.; Murty, B. S.; Wilde, G.; Divinski, S. V. Ni tracer diffusion in CoCrFeNi and CoCrFeMnNi high entropy alloys. *J. Alloys Compd.* **2016**, *688*, 994–1001.

[47] Vaidya, M.; Pradeep, K. G.; Murty, B. S.; Wilde, G.; Divinski, S. V. Bulk tracer diffusion in CoCrFeNi and CoCrFeMnNi high entropy alloys. *Acta Mater.* **2018**, *146*, 211–224.

[48] Chen, W. M.; Zhang, L. J. High-throughput determination of interdiffusion coefficients for Co-Cr-Fe-Mn-Ni high-entropy alloys. *J. Phase Equilib. Diffus.* **2017**, *38*, 457–465.

[49] Kottke, J.; Utt, D.; Laurent-Brocq, M.; Fareed, A.; Gaertner, D.; Perrière, L.; Rogal, Ł.; Stukowski, A.; Albe, K.; Divinski, S. V. et al. Experimental and theoretical study of tracer diffusion in a series of (CoCrFeMn)$_{100-x}$Ni$_x$ alloys. *Acta Mater.* **2020**, *194*, 236–248.

[50] Zhang, J. F.; Gadelmeier, C.; Sen, S.; Wang, R.; Zhang, X.; Zhong, Y.; Glatzel, U.; Grabowski, B.; Wilde, G.; Divinski, S. V. Zr diffusion in BCC refractory high entropy alloys: A case of 'non-sluggish' diffusion behavior. *Acta Mater.* **2022**, *233*, 117970.

[51] Sen, S.; Zhang, X.; Rogal, L.; Wilde, G.; Grabowski, B.; Divinski, S. V. "Anti-sluggish" Ti diffusion in HCP high-entropy alloys: Chemical complexity vs. *lattice distortions. Scr. Mater.* **2023**, *224*, 115117

[52] Zhang, F.; Zhang, C.; Chen, S. L.; Zhu, J.; Cao, W. S.; Kattner, U. R. An understanding of high entropy alloys from phase diagram calculations. *Calphad* **2014**, *45*, 1–10.

[53] Paul, A.; Laurila, T.; Vuorinen, V.; Divinski, S. V. *Thermodynamics, Diffusion and the Kirkendall Effect in Solids*; Springer: Cham, 2014.

[54] Beke, D. L.; Erdélyi, G. On the diffusion in high-entropy alloys. *Mater. Lett.* **2016**, *164*, 111–113.

[55] Kucza, W.; Dąbrowa, J.; Cieślak, G.; Berent, K.; Kulik, T.; Danielewski, M. Studies of "sluggish diffusion" effect in Co-Cr-Fe-Mn-Ni, Co-Cr-Fe-Ni and Co-Fe-Mn-Ni high entropy alloys; determination of tracer diffusivities by combinatorial approach. *J. Alloys Compd.* **2018**, *731*, 920–928.

[56] Gaertner, D.; Kottke, J.; Wilde, G.; Divinski, S. V.; Chumlyakov, Y. Tracer diffusion in single crystalline CoCrFeNi and CoCrFeMnNi high entropy alloys. *J. Mater. Res.* **2018**, *33*, 3184–3191.

[57] Gaertner, D.; Kottke, J.; Chumlyakov, Y.; Hergemöller, F.; Wilde, G.; Divinski, S. V. Tracer diffusion in single crystalline CoCrFeNi and CoCrFeMnNi high-entropy alloys: Kinetic hints towards a low-temperature phase instability of the solid-solution. *Scr. Mater.* **2020**, *187*, 57–62.

[58] Dąbrowa, J.; Danielewski, M. State-of-the-Art diffusion studies in the high entropy alloys. *Metals* **2020**, *10*, 347.

[59] Ma, S. G.; Zhang, S. F.; Gao, M. C.; Liaw, P. K.; Zhang, Y. A successful synthesis of the CoCrFeNiAl$_{0.3}$ single-crystal, high-entropy alloy by Bridgman solidification. *JOM* **2013**, *65*, 1751–1758.

[60] Ma, S. G.; Zhang, S. F.; Qiao, J. W.; Wang, Z. H.; Gao, M. C.; Jiao, Z. M.; Yang, H. J.; Zhang, Y. Superior high tensile elongation of a single-crystal CoCrFeNiAl$_{0.3}$ high-entropy alloy by Bridgman solidification. *Intermetallics* **2014**, *54*, 104–109.

[61] Patriarca, L.; Ojha, A.; Sehitoglu, H.; Chumlyakov, Y. I. Slip nucleation in single crystal FeNiCoCrMn high entropy alloy. *Scr. Mater.* **2016**, *112*, 54–57.

[62] Abuzaid, W.; Sehitoglu, H. Critical resolved shear stress for slip and twin nucleation in single crystalline FeNiCoCrMn high entropy alloy. *Mater. Charact.* **2017**, *129*, 288–299.

[63] Moon, J.; Jang, M. J.; Bae, J. W.; Yim, D.; Park, J. M.; Lee, J.; Kim, H. S. Mechanical behavior and solid solution strengthening model for face-centered cubic single crystalline and polycrystalline high-entropy alloys. *Intermetallics* **2018**, *98*, 89–94.

[64] Feuerbacher, M.; Würtz, E.; Kovács, A.; Thomas, C. Single-crystal growth of a FeCoCrMnAl high-entropy alloy. *Mater. Res. Lett.* **2017**, *5*, 128–134.

[65] Chen, H. Q.; Yuan, X. T.; Ren, W. L.; Peng, J. C.; Ding, B.; Zheng, T. X.; Yu, J. B.; Liaw, P. K.; Zhong, Y. B. A new single crystal high entropy alloy with excellent high-temperature tensile property. *Mater. Res. Express* **2020**, *7*, 046507.

[66] Liu, C. J.; Gadelmeier, C.; Lu, S. L.; Yeh, J. W.; Yen, H. W.; Gorsse, S.; Glatzel, U.; Yeh, A. C. Tensile creep behavior of HfNbTaTiZr refractory high entropy alloy at elevated temperatures. *Acta Mater.* **2022**, *237*, 118188.

[67] Xiao, W. C.; Liu, S. F.; Zhao, Y. L.; Kai, J. J.; Liu, X. J.; Yang, T. A novel single-crystal L1₂-strengthened Co-rich high-entropy alloy with excellent high-temperature strength and antioxidant property. *J. Mater. Res. Technol.* **2023**, *23*, 2343–2350.

[68] Gärtner, D.; Belkacemi, L.; Esin, V. A.; Jomard, F.; Fedotov, A. A.; Schell, J.; Osinskaya, Y. V.; Pokoev, A. V.; Duhamel, C.; Paul, A. et al. Techniques of tracer diffusion measurements in metals, alloys and compounds. *Diffus. Found.* **2021**, *29*, 31–73.

[69] Mehrer, H. *Diffusion in Solids: Fundamentals, Methods, Materials, Diffusion-Controlled Processes*; Springer: Berlin, 2007.

[70] Riesemeier, H.; Ecker, K.; Görner, W.; Müller, B. R.; Radtke, M.; Krumrey, M. Layout and first XRF applications of the BAMline at BESSY II. *X-Ray Spectrom.* **2005**, *34*, 160–163.

[71] Buzanich, A. G.; Radtke, M.; Yusenko, K. V.; Stawski, T.; Kulow, A.; Cakir, C. T.; Röder, B.; Naese, C.; Britzke, R.; Sintschuk, M. et al. BAMline—A real-life sample materials research beamline. *J. Chem. Phys.* **2023**, *158*, 244202.

[72] Lutz, C.; Hampel, S.; Ke, X.; Beuermann, S.; Turek, T.; Kunz, U.; Guilherme Buzanich, A.; Radtke, M.; Fittschen, U. E. A. Evidence for redox reactions during vanadium crossover inside the nanoscopic water-body of Nafion 117 using X-ray absorption near edge structure spectroscopy. *J. Power Sources* **2021**, *483*, 229176.

[73] Schuck, G.; Zisak, I. CryoEXAFS: X-ray absorption spectroscopy station with cryogenic or in-beam *operando* electrochemistry sample conditions at BESSY II. *J. Large-Scale Res Facil.* **2020**, *6*, A139.

[74] Zizak, I.; Gaal, P. The KMC-3 XPP beamline at BESSY II. *J. Large-Scale Res Facil.* **2017**, *3*, A123.

[75] Kuzmin, A.; Chaboy, J. EXAFS and XANES analysis of oxides at the nanoscale. *IUCrJ* **2014**, *1*, 571–589.

[76] XAESA. xaesa v0.06; GitHub: 2022 [Online]. https://github.com/aklnk/xaesa (accessed Mar 1, 2022).

[77] Timoshenko, J.; Kuzmin, A. Wavelet data analysis of EXAFS spectra. *Comput. Phys. Commun.* **2009**, *180*, 920–925.

[78] Timoshenko, J.; Kuzmin, A.; Purans, J. Reverse Monte Carlo modeling of thermal disorder in crystalline materials from EXAFS spectra. *Comput. Phys. Commun.* **2012**, *183*, 1237–1245.

[79] Timoshenko, J.; Kuzmin, A.; Purans, J. EXAFS study of hydrogen intercalation into ReO₃ using the evolutionary algorithm. *J. Phys. Condens. Matter* **2014**, *26*, 055401.

[80] Ankudinov, A. L.; Ravel, B.; Rehr, J. J.; Conradson, S. D. Real-space multiple-scattering calculation and interpretation of X-ray-absorption near-edge structure. *Phys. Rev. B* **1998**, *58*, 7565–7576.

[81] Rehr, J. J.; Albers, R. C. Theoretical approaches to X-ray absorption fine structure. *Rev. Mod. Phys.* **2000**, *72*, 621–654.

[82] Li, K. M.; Fu, C. C.; Nastar, M.; Soisson, F. Predicting atomic diffusion in concentrated magnetic alloys: The case of paramagnetic Fe-Ni. *Phys. Rev. B* **2023**, *107*, 094103.

[83] Cowley, J. M. An approximate theory of order in alloys. *Phys. Rev.* **1950**, *77*, 669–675.

[84] Cowley, J. M. Short-range order and long-range order parameters. *Phys. Rev.* **1965**, *138*, A1384–A1389.

[85] Sugita, K.; Matsuoka, N.; Mizuno, M.; Araki, H. Vacancy formation enthalpy in CoCrFeMnNi high-entropy alloy. *Scr. Mater.* **2020**, *176*, 32–35.

[86] Huang, E. W.; Chou, H. S.; Tu, K. N.; Hung, W. S.; Lam, T. N.; Tsai, C. W.; Chiang, C. Y.; Lin, B. H.; Yeh, A. C.; Chang, S. H. et al. Element effects on high-entropy alloy vacancy and heterogeneous lattice distortion subjected to quasi-equilibrium heating. *Sci. Rep.* **2019**, *9*, 14788.

[87] Ravel, B. The Athena: A User's Guide. https://bruceravel.github.io/demeter/aug/ (accessed Jun 1, 2023).

[88] Hobbs, D.; Hafner, J.; Spišák, D. Understanding the complex metallic element Mn. I. Crystalline and noncollinear magnetic structure of α-Mn. *Phys. Rev. B* **2003**, *68*, 014407.

[89] Oh, H. S.; Kim, S. J.; Odbadrakh, K.; Ryu, W. H.; Yoon, K. N.; Mu, S.; Körmann, F.; Ikeda, Y.; Tasan, C. C.; Raabe, D. et al. Engineering atomic-level complexity in high-entropy and complex concentrated alloys. *Nat. Commun.* **2019**, *10*, 2090.

[90] Li, Q.; Chen, W. M.; Zhong, J.; Zhang, L. J.; Chen, Q.; Liu, Z. K. On sluggish diffusion in Fcc Al-Co-Cr-Fe-Ni high-entropy alloys: An experimental and numerical study. *Metals* **2018**, *8*, 16.

[91] Jin, K.; Zhang, C.; Zhang, F.; Bei, H. B. Influence of compositional complexity on interdiffusion in Ni-containing concentrated solid-solution alloys. *Mater. Res. Lett.* **2018**, *6*, 293–299.

[92] Park, N.; Lee, B. J.; Tsuji, N. The phase stability of equiatomic CoCrFeMnNi high-entropy alloy: Comparison between experiment and calculation results. *J. Alloys Compd.* **2017**, *719*, 189–193.

[93] Ikeda, Y.; Grabowski, B.; Körmann, F. *Ab initio* phase stabilities and mechanical properties of multicomponent alloys: A comprehensive review for high entropy alloys and compositionally complex alloys. *Mater. Charact.* **2019**, *147*, 464–511